RESEARCH ARTICLE

ADVANCED OPTICAL MATERIALS
www.advopticalmat.de

Terahertz Emission Modulation Caused by Ultrafast Breaking and Recovery of Exchange Bias

Je-Ho Shim, Yunxiu Zhao, Qoimatul Mustaghfiroh, Nguyen Le Thi, Fathiya Rahmani, Kyungwan Kim, Hee Jun Shin, Jaehun Park, Xiao You, Caihua Wan, Min-Seung Jung, Jung-Il Hong, Hong-Guang Piao, Xiufeng Han, and Dong-Hyun Kim**

Magnetic interfacial exchange bias, as a key control method for spintronic devices, remains unclear in terms of its ultrafast dynamic behavior and its role in regulating spintronic terahertz emissions. In this work, femtosecond optical pulses are used to excite ferromagnetic/antiferromagnetic bilayer films with interfacial exchange bias, and a significant modulation phenomenon of terahertz emission is observed by comparing samples with different magnetization pinning states induced by exchange bias. Through the measurement of dynamic hysteresis loops under femtosecond optical pulse excitation, it is confirmed that the optical pulse can rapidly break and then recover the exchange bias within the picosecond time scale. This transient reconstruction process of exchange bias effectively enhances the ultrafast spin precession signal at ≈2 THz, while suppressing the ultrafast demagnetization-related signal at ≈0.77 THz. By exploiting the difference in flip symmetry of the samples, this is found that the photo-introduced magnetization dynamics process dominated the modulation effect of the exchange bias on the two frequency bands. These results reveal that picosecond-scale transient exchange bias can regulate both the frequency content and coherence of spintronic terahertz emission, offering a pathway toward tunable terahertz spintronic sources.

1. Introduction

The terahertz (THz) band (0.1–10 THz), situated between the infrared and microwave regions, represents a spectral region of growing interest due to its unique applications in ultrafast spintronics,[1–6] telecommunications,[7,8] medicine,[9,10] and fundamental nanosciences.[3,6] The so-called “THz gap”, historically limited by the lack of efficient sources and detectors, has prompted significant research efforts into broadband THz emitters. Among various platforms, magnetic materials have emerged as promising candidates due to their intrinsic spin and charge dynamics.[1–6,11–28] Several key mechanisms have been identified for THz generation from magnetic materials. One major contributor is ultrafast photoinduced magnetization dynamics (PMD), wherein femtosecond optical pulses induce rapid changes in magnetization, resulting in THz emission, particularly in relatively

---

J.-H. Shim, H.-G. Piao
Department of Physics
College of Science
Yanbian University
Yanji 133002, P. R. China
E-mail: hgpiao@ybu.edu.cn

J.-H. Shim, H.-G. Piao
Institute of Quantum Science and Technology
Yanbian University
Yanji 133002, P. R. China

Y. Zhao, Q. Mustaghfiroh, N. L. Thi, F. Rahmani, K. Kim, D.-H. Kim
Department of Physics
Chungbuk National University
Cheongju 28644, South Korea
E-mail: donghyun@cbnu.ac.kr

Y. Zhao, X. You
School of Engineering
Westlake University
Hangzhou 310024, P. R. China

N. L. Thi
Faculty of Engineering
Technology
and Communication
Hong Duc University
Thanh Hoa 40000–42000, Vietnam

H. J. Shin, J. Park
Pohang Accelerator Laboratory
POSTECH
Pohang 37673, South Korea

C. Wan, X. Han
Beijing National Laboratory for Condensed Matter Physics
Institute of Physics
Chinese Academy of Sciences
Beijing 100190, P. R. China

M.-S. Jung, J.-I. Hong
Department of Emerging Materials Science
Daegu Gyeongbuk Institute of Science and Technology
Daegu 42988, South Korea

The ORCID identification number(s) for the author(s) of this article can be found under https://doi.org/10.1002/adom.202503272

DOI: 10.1002/adom.202503272

thick ferromagnetic metal films.[11–13] In parallel, spin-to-charge conversion (SCC) phenomena such as the inverse spin Hall effect (ISHE),[6,14–17] the inverse Rashba–Edelstein effect,[17–20] and the inverse spin–orbit torque[21,22] have been actively investigated, especially in ferromagnetic metal/non-magnetic metal interfaces.[6,14–20,23,24] In addition to these SCC mechanisms, the anomalous Hall effect (AHE), resulting from the transverse motion of spin-polarized electrons within the ferromagnet, has been shown to contribute to THz emission, even in single-layer ferromagnetic systems.[25–28]

Exchange bias, originating from ferromagnetic/antiferromagnetic (FM/AFM) interfacial coupling,[29–32] provides critical spin-direction control for spintronic memory devices.[33–37] Recent advances demonstrate the ultrafast optical manipulation of this material through femtosecond optical excitation, where transient electron heating induces picosecond-scale exchange bias breaking and recovery in heterostructures.[38] This non-thermal approach not only surpasses field-annealing limitations but also establishes exchange bias as a dynamically tunable state bridging ultrafast photonics and spintronic functionality.

The presence of exchange bias distinguishes FM/AFM heterostructures from conventional ferromagnetic-metal/heavy-metal (FM/HM) systems. While exchange bias has been proposed to enhance THz emission via increased magnetic anisotropy,[16] intense femtosecond excitation can significantly modify or even break exchange bias coupling.[38] Notably, ultrafast exchange-coupling torques, faster than conventional ultrafast demagnetization (UDM), have been reported,[39] suggesting the potential for active control over THz emission. Furthermore, nonequilibrium exchange interactions have emerged as key mechanisms in optically triggered spin dynamics,[40,41] reinforcing the role of FM/AFM interfaces as tunable THz sources. Nevertheless, the behavior of exchange bias under ultrafast optical excitation remains incompletely understood.

In FM/AFM systems, it has been known that the SCC contribution by AFM layer depends on its crystal quality. When the AFM forms a well-crystallized and chemically ordered phase, such as the L1_2-type IrMn$_3$ structure,[16,42] the injected spin current from the FM can propagate through the AFM, being converted into a measurable SCC signal via the inverse spin Hall effect. In contrast, when the AFM layer is a disordered alloy phase with poor crystallization, as is typically the case for sputtered films,[43,44] the AFM behaves mainly as a spin sink or produces strong spin reflection at the FM/AFM interface. It is considered that the SCC contribution is negligible for the samples fabricated by sputtering in the present study.

In this work, we directly observe the ultrafast breaking and recovery of exchange bias in Py/IrMn bilayers and establish a direct correlation with the THz emission dynamics. Time-resolved THz emission spectroscopy reveals that the transient disruption and restoration of interfacial exchange bias govern the interplay between ultrafast demagnetization and spin precession in the Py layer. Our findings demonstrate three key mechanisms of THz emission modulation through ultrafast exchange bias dynamics: (1) photoinduced breaking and recovery of interfacial exchange bias enabling mode-selective control of spin excitations on picosecond timescales; (2) tunability of THz emission through AFM thickness engineering mediated by AHE and exchange bias dynamics; and (3) revelation of interface-originated coherent spin-wave excitations that provide a unified framework beyond conventional FM-based THz generation mechanisms.

2. THz Emission

The multilayer samples in the present study are Py(10)/IrMn(t_{IrMn}) on MgO(001) substrate. The 3-nm MgO capping layer is deposited for all samples for film protection. Since both the MgO substrate and the capping layer are insulators, there is no need to consider the pumping of the charge current into the substrate or the capping layer. The t_{IrMn} represents the nanoscale thickness of the AFM layer, with a value range of 0 to 5 nm. As for the sample preparation conditions, please refer to the Experimental Section. The THz emission spectroscopy experiment was designed to investigate various THz emission mechanisms of Py/IrMn samples, as illustrated in **Figure** 1a. The specific details about the THz emission spectroscopy setup are described in the Experimental Section.

To ensure that the Py/IrMn samples were in a saturated magnetization state, a 280 Oe magnetic field H_{ext} was applied along the $-x$ axis within the plane during the experiment, as the saturation magnetic fields of all samples ranged from 35 to 180 Oe. We measured the THz emission from the front and back surfaces of the sample by flipping its orientation: for the front-side measurement, the pump beam was incident on the Py layer or the capping layer (see the top of Figure 1b); for the back-side measurement, the pump beam was incident on the IrMn layer or the substrate (see the top of Figure 1c). We define the resulting THz emission signals in the front and back cases as E_y^{front} and E_y^{back} respectively. The specific contribution of the polarization mode dispersion mechanism to the actual THz emission can be distinguished by comparing E_y^{front} and E_y^{back} signals.[27,28] Because the applied external field (280 Oe) exceeds the saturation field of the exchange-biased Py layer for all samples, so that the magnetization remains parallel with H_{ext} in both geometries. Therefore, flipping the sample does not reverse the magnetization direction but only changes the order of the Py/IrMn and Py/MgO interfaces with respect to the pump incidence and THz propagation.

The bottoms of Figures 1b,c show the variation trend of THz emission signals related to the t_{IrMn}. For the pure Py(10) sample without an IrMn layer, it can be observed that the sign of the THz emission signal flips depending on whether the pump laser is incident from the front or the back. This indicates that since the PMD signal is not affected by the sample flip, the AHE mechanism contributes to the THz signal. Interestingly, it can be observed that depositing only a 1-nm IrMn layer beneath the Py layer is sufficient to completely reverse the THz emission signal of E_y^{front}, and the same is true for E_y^{back}, as shown by the comparison of the black and colored lines at the bottom of Figures 1b,c.

3. The AHE Signal Inversion

To understand the reasons for the above-mentioned THz emission trends, it is necessary to quantitatively separate the potential THz emission mechanisms, as shown in Figures 1b,c. For a pure Py sample, the THz emission data can be analyzed di-

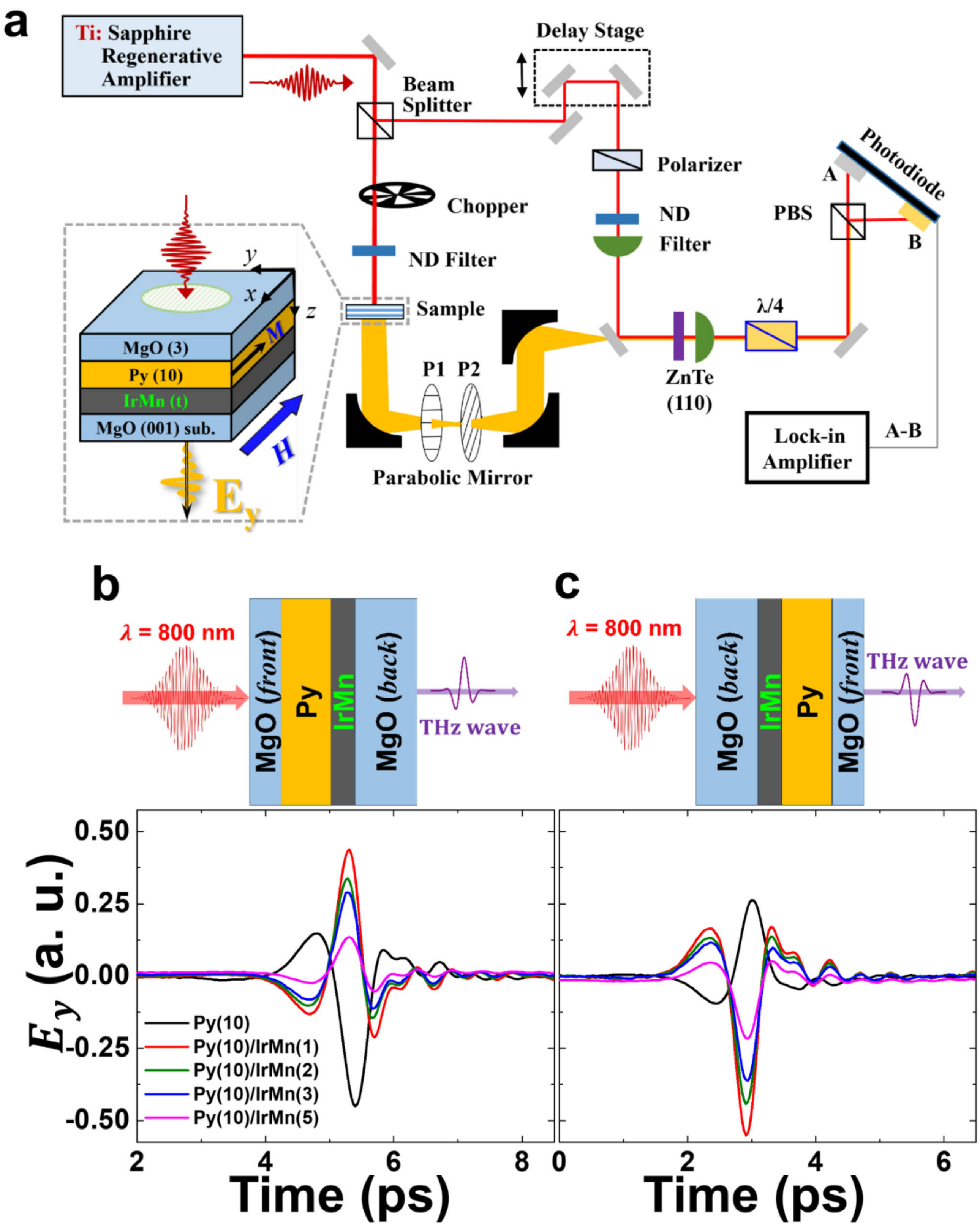

Figure 1. a) The THz emission spectroscopy setup schematic diagram. THz emission waveform when the pump laser is toward the b) front and c) back surfaces of Py(10)/IrMn(t_{IrMn}) with $t_{\mathrm{IrMn}} = 0$, 1, 2, 3, and 5 nm.

rectly. However, when IrMn is introduced, it is necessary to consider the absorption of the IrMn layer for THz waves (for the front case) and the pump laser (for the back case), and the signal must be corrected accordingly. In **Figure 2**, the corrected THz signals (Exp.) used for the AHE/PMD decomposition correspond to $(\beta_{front}^{THz}[t])^{-1} E_y^{front}[t]$ and $(\beta_{back}^{Pulse}[t])^{-1} E_y^{back}[t]$. Here, "front" and "back" denote whether the optical pump pulse is incident on the front side or the back side of the sample, respectively. $\beta_{front}^{THz}[t]$ compensates the attenuation of the emitted THz wave as it propagates through the IrMn layer in the front-incident configuration, whereas $\beta_{back}^{Pulse}[t]$ compensates the absorption of the optical pump pulse by the IrMn layer in the back-incident configuration.

Using these correction factors, the PMD (symmetric) and AHE (asymmetric) components of the THz emission are obtained through the following relations:

$$2E_y^{PMD}[t] = \left(\beta_{front}^{THz}[t]\right)^{-1} E_y^{front}[t] + \left(\beta_{back}^{Pulse}[t]\right)^{-1} E_y^{back}[t] \quad (1)$$

$$2E_y^{AHE}[t] = \left(\beta_{front}^{THz}[t]\right)^{-1} E_y^{front}[t] - \left(\beta_{back}^{Pulse}[t]\right)^{-1} E_y^{back}[t] \quad (2)$$

Equation (1) yields the PMD contribution, which maintains the same phase under front and back pumping, while Equation (2) isolates the AHE contribution, which undergoes a 180° phase reversal upon flipping the pump incidence direction. The detailed derivation and the IrMn-thickness–dependent coefficients are provided in Section S1 (Supporting Information).

Figure 2 compares the THz emission characteristics and their physical mechanisms of pure Py(10) and Py(10)/IrMn(1) samples. In the left columns of Figure 2, the variations of E_y^{front} and E_y^{back} overtime for both samples are presented. Here, the black dashed lines represent the corrected experimental signals of THz emission, which are composed of contributions from PMD (red lines) and AHE (blue lines). Due to the dependence of PMD and AHE signals on the symmetry of the sample structure, that is, when the laser is incident on the sample from the front and back, they exhibit symmetrical and asymmetrical characteristics, respectively. Therefore, these two signals can not only be separated by flipping the samples, but also, as shown by the blue and red lines in this Figure, it can be observed that AHE is the main contributing factor to the reversal of THz emission signals. We emphasize that the external magnetic field remains applied during all measurements. The separation between AHE and PMD relies solely on their opposite flipping symmetries (AHE: antisymmetric, PMD: symmetric), and therefore does not require switching the external field. It is well known that THz signals generated by spin-orbit coupling mechanisms, such as the inverse spin Hall effect, can occur at the interfaces of ferromagnetic materials. However, in our case, the MgO layer being an insulator at the Py/MgO interface effectively suppresses this effect. Additionally, at the Py/IrMn interface, the IrMn layer acts as an effective spin sink layer,[43,44] making its contribution negligible. Since the THz emission polarization is along the y direction, the contribution of the inverse spin–orbit torque can be excluded.[17] In our measurements, it was observed that the measured E_x-component was negligible within the noise level when the pump beam helicity changed, indicating that the inverse spin-orbit torque also did not make a significant contribution.

The experimental results in Figure 2 show that the THz emission signal can be reversed by flipping the sample. The introduction of only a 1-nm IrMn layer is sufficient to reverse the sign of the THz emission. By analyzing the separated signals, it is confirmed that the contribution of the AHE (blue line) is the leading cause of this signal reversal. Note that all the PMD signs remain the same regardless of sample flipping and addition of IrMn layer, which can be explained by the THz waves caused by E_y^{PMD} that depends only on magnetization dynamics, that is, according to the relationship $E_y^{PMD}[t] = \frac{\mu_0}{4\pi^2 r}\frac{\partial^2 M_x}{\partial t^2}$.[11,12] In addition, although the PMD signal extracted from Py(10)/IrMn(1) is significantly weaker than that of pure Py, it contains a waveform with a higher THz frequency. We will further discuss this in detail in Figure 4.

The generation mechanism of the THz emission signals for pure Py(10) and Py(10)/IrMn(1) samples induced by AHE is illustrated in the right column of Figure 2. For pure FM samples, previous studies have shown that the AHE direction in insulator/FM/insulator structures is determined by the difference in the photoinduced current reflected at both FM/insulator interfaces with different roughness.[25] In Figures 2a,b, our case resembles the above phenomenon, the effective current density j_c^{back} at the substrate interface is larger than j_c^{front} at the capping interface. This is attributed to the lower roughness of the back interface compared to the front interface, as the interface generally deposited by magnetron sputtering is not as smooth as the substrate. Therefore, due to the difference in interface roughness between the capping layer and the substrate, a photoinduced current difference is inevitably generated at the interfaces on both sides of Py, induced by the AHE. Thus, in our samples, the photoexcited current j_c^{back} produced at the substrate interface becomes dominant. All arrows shown in Figures 2 and 3 represent the charge-current direction, which is opposite to the actual electron propagation direction.

However, it is interesting that the insertion of a mere 1 nm-IrMn layer causes the AHE signal to reverse, as compared between pure Py(10) and Py(10)/IrMn(1) samples, as shown in Figures 2a,c, as well as Figures 2b,d. Clearly, this indicates that even without considering the interface roughness, due to the difference in electrical conductivity between the insulator MgO and the alloy IrMn, there must be a difference in the reflectivity of photoinduced electrons at the interfaces on both sides of Py. Therefore, the reflectivity of photoinduced electrons at the Py/IrMn interface must be lower than that at the Py/MgO interface. As a result, the effective AHE current direction is determined by the photoinduced current j_c^{front} at the front interface MgO/Py, as illustrated in the right columns of Figures 2c,d. Therefore, in our samples the AHE-induced THz emission can be described by the following relationship: $E_y^{AHE} \sim \theta_{AHE}\boldsymbol{m} \times (j_c^{front} + j_c^{back})$.[25–28]

4. IrMn Thickness-Dependent AHE

Figure 3 analyzes the AHE characteristics and their physical mechanisms of Py(10)/IrMn(t_{IrMn}) samples with different IrMn thicknesses. As shown in Figure 3a, by comparing the THz emission induced by AHE in various samples, it is found that although the THz emission intensity suddenly increases when a 1 nm-

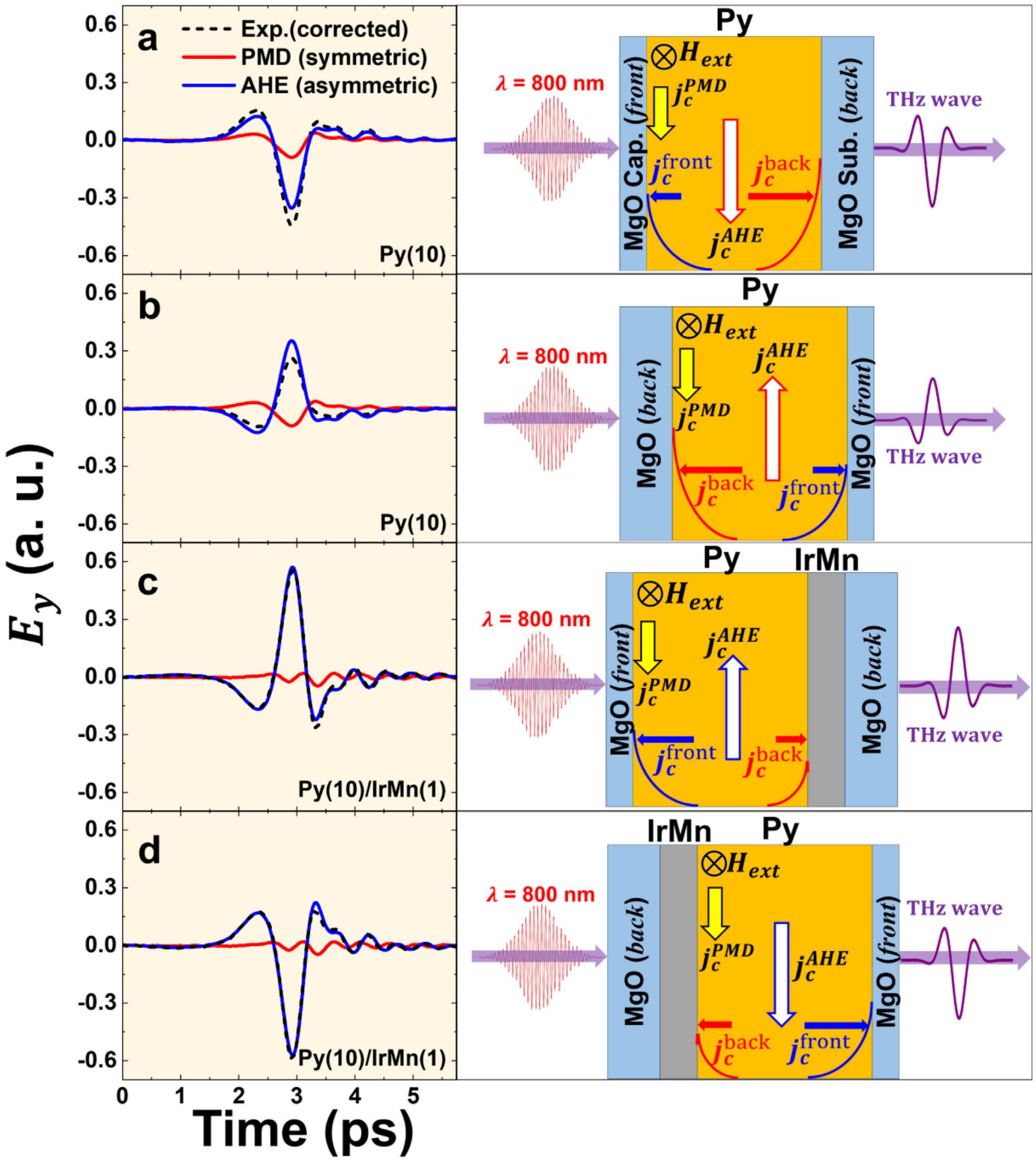

Figure 2. In the left column, corrected THz emission waveforms (black dashed line) after absorption compensation, which decomposed into AHE (blue) and PMD (red). The corrected experimental signals (Exp.) correspond to $(\beta_{front}^{THz}[t])^{-1} E_y^{front}[t]$ and $(\beta_{back}^{Pulse}[t])^{-1} E_y^{back}[t]$, representing the absorption-compensated front-side and back-side THz emission traces used in the AHE/PMD decomposition. The derivation of the correction factors is given in Section S1 of the Supporting Information. In case of a) front and b) back side pumping for pure Py(10). In case of c) front and d) back side pumping for Py(10)/IrMn(1). The mechanism is schematically illustrated for (a–d) cases in the right column. The H_{ext} is applied along the -x axis within the plane. j_c^{front} (blue arrows) represents the reflected current from the MgO(front)/Py interface; j_c^{back} (red arrows) represents the reflected current from the Py/MgO(back) or Py/IrMn interface; j_c^{AHE} (white hollow arrows) represents the charge current generated by AHE in the Py layer; j_c^{PMD} (yellow hollow arrows) represents the charge current induced by PMD. All arrows indicate the charge-current direction (opposite to the actual electron propagation direction).

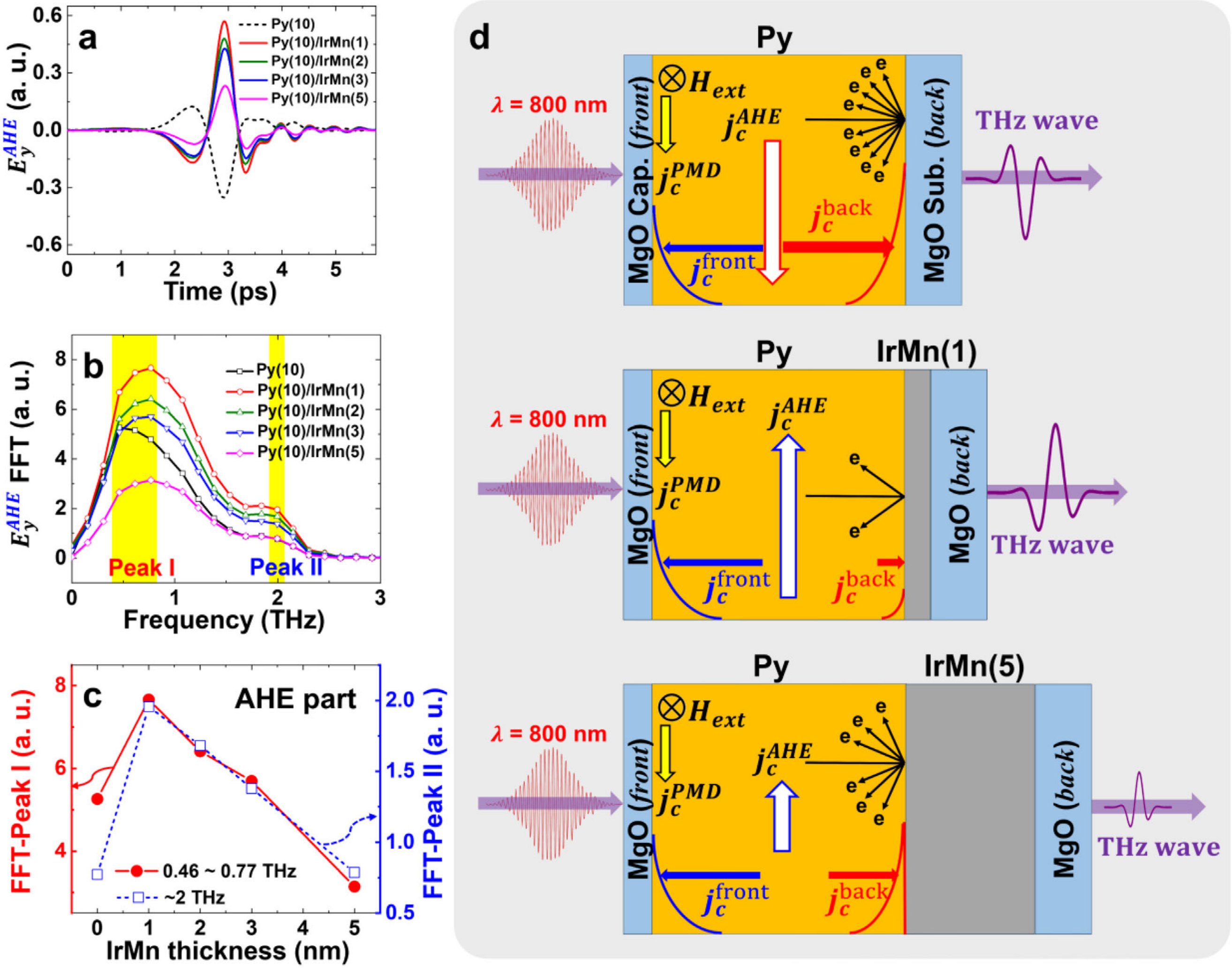

Figure 3. For Py(10)/IrMn(t_{IrMn}) with $t_{\mathrm{IrMn}} = 0$, 1, 2, 3, and 5 nm: a) E_y^{AHE} versus time, b) FFT for E_y^{AHE}, and c) FFT peak I (red line) and peak II (blue dashed line) of E_y^{AHE}. d) Schematic diagram of the dependence of the photoinduced current in samples with different t_{IrMn} on the electron reflectivity (back arrows) at the Py/IrMn interface. j_c^{front}, j_c^{back}, j_c^{AHE}, and j_c^{PMD} refer to Figure 2. All arrows represent the charge-current direction, which is opposite to the electron motion.

IrMn layer is inserted, it shows a decreasing trend as the thickness of t_{IrMn} continues to increase. Since we have already performed absorption compensation for the E_y^{AHE} data (Section S1, Supporting Information), the signal weakening with the increase in the thickness of the IrMn layer is not caused by the absorption of the IrMn layer.

To further investigate this trend, fast Fourier transforms (FFTs) were applied to the THz emission signals in Figure 3a. As shown in Figure 3b, two peaks of THz emission induced by the AHE can be clearly observed in the FFT curves of all samples. Here, the peak I, as the dominant frequency, is located in the region near 0.77 THz. Its amplitude significantly decreases with the increase of t_{IrMn}, which is attributed to the photoinduced AHE. Additionally, it is found that in the pure Py sample, this peak slightly shifts to a lower frequency (≈0.46 THz), which can be attributed to the absence of the Py/IrMn interface effect. Among all the samples, the FFT peak II was observed in the region near 2 THz. Under the optical pulse width conditions used in our experiments, the photoinduced THz signals generally appear ≈0.77 THz. In contrast, the ≈2 THz component is observed at later delay times than the ≈0.77 THz mode (Section S3, Supporting Information), indicating that it becomes active during the post-demagnetization stage. Such behavior is consistent with a remagnetization-driven recovery of the exchange stiffness, where the transient restoring torque produces THz-frequency spin-precessional motion. The ~2 THz frequency reflects the characteristic exchange-interaction timescale, rather than conventional spin-wave propagation. Although the intensity of peak II showed the same variation trend as that of peak I with the increase of IrMn thickness, its frequency value remained relatively unchanged. This behavior confirms that the THz amplitude is governed by the imbalance between the two counter-directed

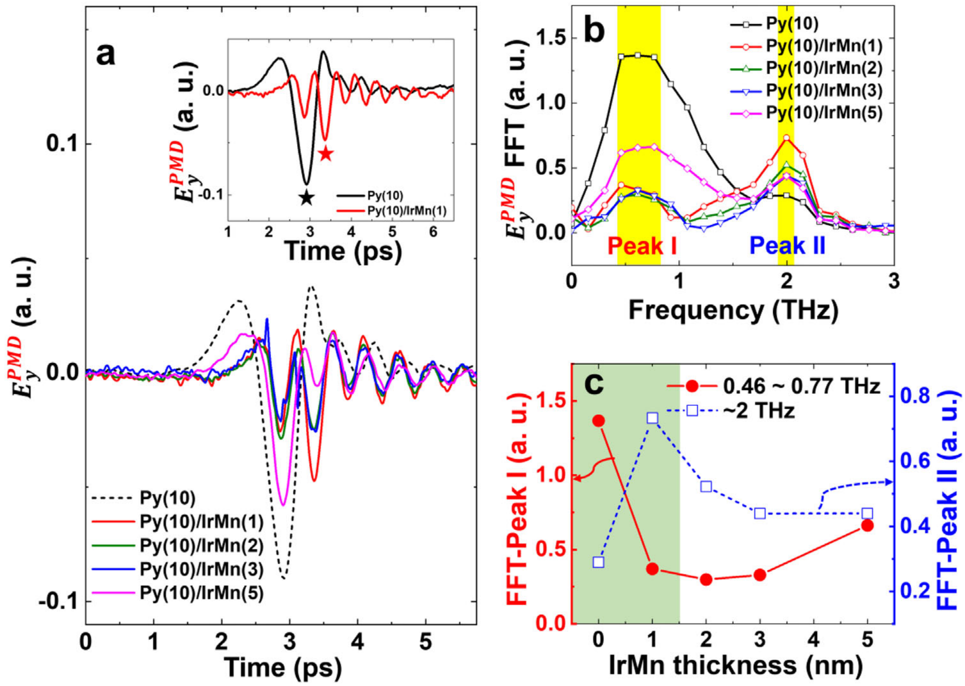

Figure 4. For Py(10)/IrMn(t_{IrMn}) with $t_{\mathrm{IrMn}} = 0$, 1, 2, 3, and 5 nm: a) E_y^{PMD} versus time, b) FFT for E_y^{PMD}, and c) FFT peak I (red line) and peak II (blue dashed line) of E_y^{PMD}. Inset of (a) is the E_y^{PMD} comparison between Py(10) (black) and Py(10)/IrMn(1) (red) over time. The black and red stars marked the THz signal peaks for Py(10) and Py/IrMn(1) samples.

interface-reflected currents, j_c^{front} from the MgO/Py interface and j_c^{back} from the Py/IrMn interface. Because the pump direction only inverts the polarity of the emitted field, the magnitude of the THz emission is determined by the difference $|j_c^{front} - j_c^{back}|$, independent of the pumping geometry.[25–28]

In Figure 3c, the variation trends of the two FFT peaks under different t_{IrMn} conditions are presented. It is found that both peaks exhibit a similar trend, increasing first and then decreasing with the increase in t_{IrMn}. Notably, when $t_{\mathrm{IrMn}} = 1$ nm, the peaks reach their maximum values and then exhibit a monotonically decreasing trend as t_{IrMn} increases further. According to relevant studies,[45] the THz emission based on SCC should enhance with the increase of t_{IrMn}. However, no such increase is observed in the asymmetric THz component. Instead, its amplitude decreases monotonically with t_{IrMn}, matching the IrMn-thickness dependence expected for an AHE-driven interfacial-reflection mechanism rather than the increasing trend predicted for SCC-driven THz emission.[45] Thus, the asymmetric contribution isolated by Equation (2) can be attributed to the AHE mechanism. Considering the dependence of AHE on the interfaces on both sides of Py,[25–28] since the dominant current j_c^{front} at the Py/MgO (capping) interface remains unchanged, the variation of E_y^{AHE} must be modulated by t_{IrMn}-dependent j_c^{back} at the Py/IrMn/MgO (substrate) interface.

Figure 3d illustrates how the photoinduced current is modified by the IrMn thickness through the reflectivity of charge current generated in the Py layer at the Py/IrMn interface. Previous studies on FM/AFM heterostructures have shown that this interfacial reflectivity increases as the AFM layer becomes thicker.[46–48] This trend explains the behavior in Figure 3c: as t_{IrMn} increases, the enhanced reflection of these FM-originated photo-induced electrons increases the back-flow current j_c^{back}, which reduces the net AHE-related current in the Py layer and leads to the monotonic decrease of the FFT peak amplitudes. Since the Py/MgO interface is an insulating boundary with intrinsically much higher reflectivity than the metallic Py/IrMn interface, the reflected-current polarity is determined primarily by the Py/MgO side. Even though the reflectivity at the Py/IrMn interface increases with IrMn thickness, it never exceeds that of the Py/MgO interface. As a result, only a single polarity reversal occurs, and no secondary reversal appears as t_{IrMn} increases. That is, as the thickness of the AFM layer increases, the reflectivity of electrons at the FM/AFM interface will increase, thereby effectively reducing the spin Hall resistance value. In our Py(10)/IrMn(t_{IrMn}) samples, as the t_{IrMn} increases, the reflection of the photoinduced electrons from the Py layer at the Py/IrMn interface will also increase. Therefore, as the t_{IrMn} increases, j_c^{back} dependent on the reflection at the Py/IrMn interface will also increase, which is precisely the fact shown by the monotonically decreasing trend of the two peaks in the FFT in Figure 3c. Similarly, when the IrMn layer as a metallic alloy is inserted between Py and the MgO substrate, the reflectivity of the photoinduced electrons will sharply decrease, causing E_y^{AHE} to reverse immediately (see Figure 2). Because the reflectivity of the MgO substrate as an insulator for the photoinduced electrons is greater than that at the Py(10)/IrMn(1) interface, as shown in the upper part of Figure 3d. Therefore, as shown in the lower part of Figure 3d, as the t_{IrMn} increases, the photoinduced current j_c^{back} on the Py/IrMn side will increase, thereby causing the E_y^{AHE} signal to gradually weaken after reversing. Since the reflectivity at the Py/IrMn interface will never exceed that at the Py/MgO interface, the reversed E_y^{AHE} signal will not reverse again with the change in the thickness of IrMn.

5. IrMn Thickness-Dependent PMD

To comprehensively understand the THz emission dynamics at the FM/AFM interface, in addition to the contribution of the AHE to THz emission discussed in the previous section, the contribution of the PMD will be further analyzed here. **Figure** 4a shows the variation of the THz emission signals E_y^{PMD} over time caused by PMD at different t_{IrMn} conditions. It is observed that the t_{IrMn} variation affects the waveform profile of E_y^{PMD}. As shown in the inset of Figure 4a, inserting a 1-nm IrMn layer clearly modifies the PMD waveform. In pure Py(10), the early-time peak (peak I; ≈0.77 THz) is strong and dominant. In Py(10)/IrMn(1), this initial peak is strongly suppressed, and the subsequent peak (peak II; ≈2 THz) becomes the main feature. Because peak II intrinsically appears after peak I (Section S3, Supporting Information), the dominant maximum is shifted to a later delay time, resulting in an effective delay of several hundred femtoseconds. Thus, the IrMn insertion leads to a redistribution of PMD amplitudes and a corresponding temporal shift of the dominant PMD peak.

To further analyze the effect of IrMn on PMD dynamics, we performed fast Fourier transforms (FFT) of E_y^{PMD}, as shown in Figure 4b. It is clearly visible in the FFT spectra that all samples exhibit two frequency peaks near 0.77 THz and 2 THz, which are respectively associated with the UDM (ultrafast demagnetization; peak I) and USP (ultrafast spin precession; peak II) components of the THz emission. Here, USP denotes a transient terahertz-frequency precessional response that appears as the exchange interaction begins to recover during the ultrafast remagnetization stage. These peak positions are basically consistent with those observed in the AHE case, which might be attributed to the common temporal excitation of the femtosecond pump pulses on them. However, unlike in the AHE, with the t_{IrMn} increase, the relative intensity evolution of the two peaks shows a significantly different trend.

As can be observed from Figure 4c, when the thickness of the IrMn layer increases from 0 to 1 nm (green-shaded area), the intensity of peak I near 0.77 THz is significantly suppressed, while peak II near 2 THz is greatly enhanced. For thicker IrMn layers, as t_{IrMn} increases, peak I shows a gradually recovering trend, while peak II continues to decrease. This opposite behavior of the two peaks indicates a substantial reorganization of the PMD modes at the FM/AFM interface. This results that the insertion of IrMn layer leads to an alteration of the PMD dynamics in Py layer. The overall FFT trend in Figure 4c, especially the decoupling of the intensity evolution of peak I and peak II, contrasts sharply with the behavior observed in the AHE-induced signal.

6. Comparison of Hysteresis Loops of Static and Ultrafast Dynamic States

To explore the correlation between the exchange bias[49] at the Py(10)/IrMn(t_{IrMn}) interface and the ultrafast PMD, we extracted the THz peak amplitude at a fixed delay time in the front-incidence geometry while sweeping the external magnetic field, and constructed the hysteresis loops for the ultrafast dynamic state. The static hysteresis loops were measured using a vibrating sample magnetometer, and both sets of loops were normalized for direct comparison. As shown in **Figure** 5a, the static and ultrafast hysteresis loops are almost identical for the pure Py sample, indicating that the optical excitation does not alter the magnetic structure in the absence of an AFM layer. When IrMn is introduced, however, the ultrafast loops deviate from the static ones, demonstrating that the Py/IrMn interface modifies the magnetic configuration during ultrafast excitation. For t_{IrMn} = 1 nm (Figure 5b), the ultrafast loop shows only a small reduction in slope near 0 Oe, implying a weak modification of the interfacial spin configuration. In contrast, for t_{IrMn} = 3 and 5 nm (Figures 5c,d), the static loops clearly exhibit exchange bias, whereas the ultrafast loops show no shift (t_{IrMn} = 3 nm) or a substantially reduced shift (t_{IrMn} = 5 nm). This behavior confirms that ultrafast optical excitation transiently suppresses the interfacial exchange bias, i.e., exchange-bias breaking (EBB). In the t_{IrMn} = 5 nm sample, a small remanent bias (≈−20 Oe) remains, indicating that the EBB is not fully complete. Comparing t_{IrMn} = 3 and 5 nm shows that a thicker IrMn layer is less favorable for achieving complete EBB. We note that the static and dynamic hysteresis loops of the Py/IrMn samples display a slight asymmetry (Figures 5c,d). Such non-ideal loop shapes may arise from several sample-dependent factors, including minor-loop or partial-training behavior of the interfacial AFM moments, the multiphase nature of IrMn, or microstructural asymmetry introduced during magnetron sputtering. These effects can influence the detailed loop profile, but they do not obscure the shift of the loop center, which is the quantity used in this work to identify ultrafast exchange-bias breaking (EBB) under optical excitation.

7. Tunable THz Emission Caused by Ultrafast Exchange Bias Dynamics

Based on the above discussion and analysis, it can be determined that AHE and PMD play the leading roles in our THz emission system. Among them, the low-frequency THz signal (peak I) is contributed by UDM and AHE, while USP contributes the high-frequency THz signal (peak II). The ≈2 THz component (peak II) that appears in the AHE-isolated THz signal does not originate from AHE-related dynamics. It reflects the USP mode driven by the exchange-restoring torque acting on the entire excited region. Because this ultrafast precessional response is embedded in the total THz waveform, it is inherited by both the PMD- and AHE-separated signals. Therefore, it is essential to further analyze in detail the contribution of PMD caused by ultrafast exchange bias dynamics to the THz emission mechanism. Consistent with the inset of Figure 4a and with the mode-resolved analysis in Section 3 of the Supporting Information, the component associated with peak I (≈0.77 THz) reaches its maximum earlier, whereas the component associated with peak II (≈2 THz) becomes dominant at a later delay time. This description follows the envelope-based interpretation of the PMD dynamics and preserves the intrinsic temporal ordering of the two modes. This means that when the femtosecond pulsed laser excites our sample, the PMD

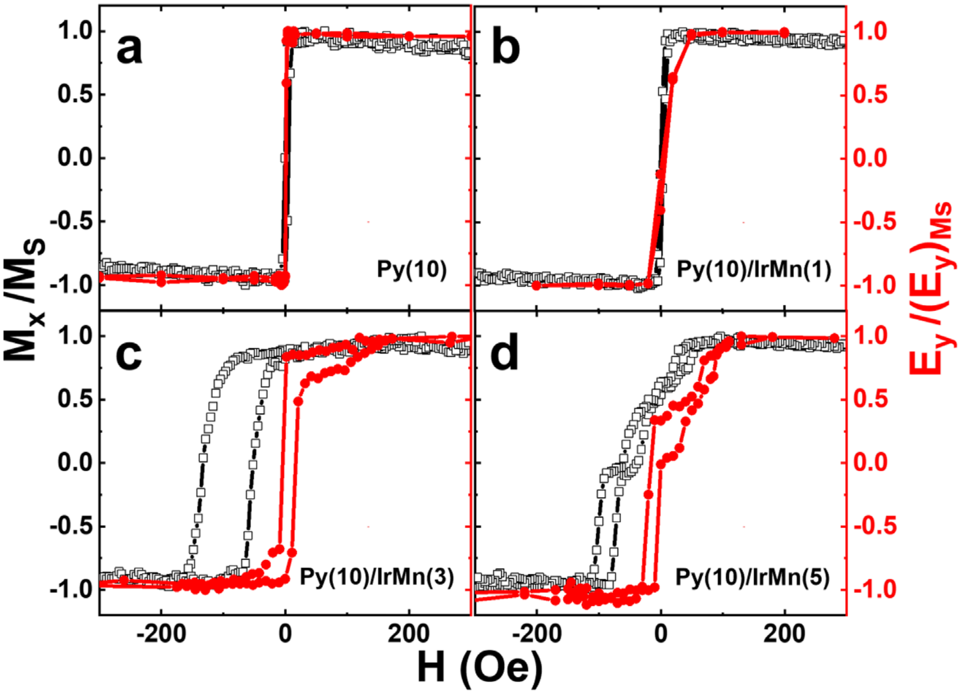

Figure 5. Normalized static hysteresis loops (black open circles) and THz emission peak hysteresis loops (red closed circles) for a) Py(10), b) Py(10)/IrMn(1), c) Py(10)/IrMn(3), and d) Py(10)/IrMn(5), respectively.

process of the magnetic system can be further divided along the time axis into the appearance of UDM first, followed by USP.

To more intuitively reveal the influence mechanism of ultrafast exchange bias dynamics on PMD in the Py/IrMn heterostructure system, we depict the time evolution of the spin configurations on a picosecond timescale and schematically compare the physical mechanisms of pure Py and Py/IrMn systems in Figure 6. The left side of Figure 6 illustrates the PMD evolution process of the spin configurations at the laser spot of a pure Py sample over time when it is excited by femtosecond optical pulses. When a ≈1 ps optical pulse irradiates the sample, the spin order within the excited region becomes instantaneously disordered due to the ultrafast electron excitation and the resulting nonthermal electron induced spin scattering,[50] thereby inducing the UDM mode (≈0.77 THz). After the optical pulse irradiation, the exchange interaction recovers on a picosecond timescale. During this recovery process, a short-lived high-frequency precessional response is generated, giving rise to the ≈2 THz USP component.

The time evolution of PMD observed in pure Py, that is, the appearance of UDM (peak I) followed by USP (peak II) on the picosecond timescale, was consistently reproduced in the Py/IrMn sample series, as shown in the right side of Figure 6. However, unlike in pure Py, the PMD in the Py/IrMn system is inevitably affected by the exchange bias dynamics occurring at the Py/IrMn interface, as shown in Figures 4 and 5. When the optical pulse irradiates for ≈1 ps, the EBB at the Py/IrMn interface suppresses the UDM mode in the Py layer. As t_{IrMn} increases, the static exchange bias at the Py/IrMn interface strengthens (Figure 5), which makes the interfacial AFM configuration more difficult to fully disorder under the same pump fluence. As a result, the UDM suppression and the associated enhancement of the USP mode decrease for thicker IrMn layers (Figure 4c). This evolution reflects a reduction in the efficiency of ultrafast exchange-bias breaking (EBB), whereas the central frequencies of the UDM and USP components remain unchanged, as indicated by the FFT spectra in Figure 4. These exchange bias dynamics also affect the USP mode, which is intrinsically related to the reordering of spins. After EBB occurs at the Py/IrMn interface, the AFM spins in the IrMn layer will subsequently be reordered under the assistance of an external magnetic field, a process we refer to as exchange-bias recovery (EBR). The EBR process will lead to a more ordered reconstruction of spins in the Py layer, thereby enhancing the USP mode on a timescale of several picoseconds. It should be emphasized that the USP mode cannot be observed in the pure IrMn system under optical pulse excitation (see Section S2, Supporting Information), while in the Py/IrMn structure, due to the presence of EBB and EBR processes, not only can the USP mode be observed, but also enhanced. As shown in Figures 4b,c, the degree of EBR (see peak II) is directly affected by the degree of the previously occurring EBB (see peak I). An enhanced EBB will necessarily strengthen the EBR, leading to an enhanced USP mode. Therefore, when EBB strongly suppresses the UDM mode, the subsequent EBR will enhance the USP mode. This negative correlation between the suppression of UDM (see peak I) and the enhancement of USP (see peak II) with the variation of IrMn layer thickness does not exist in the pure Py system, as can be seen by comparing Figures 3b and 4b. Therefore, in the Py/IrMn system, the balance between these two ultrafast spin modes can be effectively tuned by controlling the thickness of the IrMn layer.

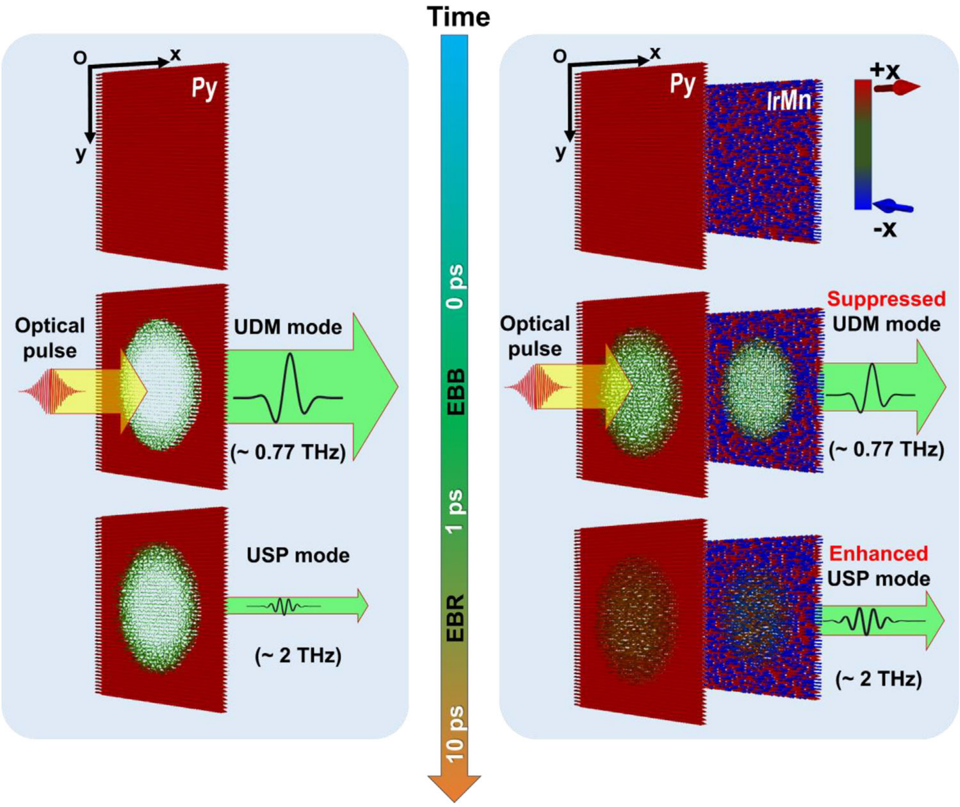

Figure 6. Schematic representation of the ultrafast THz-emission mechanisms mediated by PMD in pure Py (left) and Py/IrMn (right). The snapshots schematically indicate how UDM (≈0.77 THz) and USP (≈2 THz) modes affect the spin configuration at the laser-irradiated spot during different post-pulse time regimes. The middle panels correspond to the early (0–1 ps) exchange-bias-breaking (EBB) stage, while the bottom panels depict the later (1–10 ps) exchange-bias-recovery (EBR) stage, where USP is enhanced in Py/IrMn. The color bar schematically indicates variations of the spin direction along the x-axis.

8. Conclusion

In conclusion, we have demonstrated that THz emission in Py/IrMn systems originates from two fundamentally distinct mechanisms, namely AHE and PMD. In our system, the AHE is mainly attributed to the reflectivity of photoinduced electrons at the Py/IrMn interface, which depends on the IrMn thickness. It is worth emphasizing that PMD exhibits a dependence on ultrafast exchange bias dynamics. The experimental results show that, as the two basic modes of PMD, the contributions of UDM and USP in the process of generating THz signals have a sequential relationship, and both are affected by the dynamics of EBB and EBR, which depend on the IrMn thickness at the Py/IrMn interface. The ultrafast control effect of EBB and EBR on the spin order at the Py/IrMn interface can be utilized to tune the intensity distribution of the two frequency modes in the THz signal. Our research provides a useful platform for exploring tunable THz spintronic phenomena in FM/AFM heterostructures.

9. Experimental section

THz Emission Experiment: The THz emission measurements were conducted at the Pohang Accelerator Laboratory in South Korea. A femtosecond optical pulse was generated by an amplified Ti:sapphire laser with a central wavelength of 800 nm, a bandwidth of 20 nm, a pulse duration of 120 fs, and a repetition rate of 1 kHz. The pump laser spot size was ≈5 mm, with a fluence of 1.6 mJ cm^{-2}. A 1-mm-thick ZnTe crystal was used to detect the THz signal via electro-optic sampling. The time-domain THz emission experiment was performed using a femtosecond laser pump under an in-plane external magnetic field of 280 Oe. The schematic diagram of the experimental setup is shown in Figure 1a.

Sample Fabrication: The following samples by magnetron sputtering were fabricated: substrate MgO (001)/IrMn (t_{IrMn} nm)/Ni$_{80}$Fe$_{20}$ (Py, 10 nm)/MgO (3 nm), substrate MgO (001)/IrMn (10 nm)/MgO (3 nm), and substrate MgO (001)/Ni$_{80}$Fe$_{20}$ (Py, 10 nm)/MgO (3 nm). MgO serves as a capping layer to prevent oxidation. The field cooling method was used to establish the exchange bias by applying an in-plane magnetic field of 1 kOe while cooling the sample from 750 K (above the Néel temperature of IrMn) to ≈300 K.

Supporting Information

Supporting Information is available from the Wiley Online Library or from the author.

Acknowledgements

J.H.S. and Y.Z. contributed equally to this work. They collaboratively designed the experimental framework, carried out the data analysis, jointly interpreted the results, and prepared the manuscript. Q.M., N.L.T., and F.R. assisted with the THz measurements. H.J.S. and J.P. were responsible for establishing the THz experimental setup. M.-S.J., J.-I.H., C.W., and X.H. fabricated the multilayer samples and conducted their structural and magnetic characterizations. X.Y. and K.K. offered valuable experimental insights and suggestions. H.-G.P. and D.-H.K. supervised the overall project and critically reviewed the manuscript as corresponding authors. This research was supported by the National Natural Science Foundation of China (Grant No. 12364020), Basic Science Research Program through the National Research Foundation of Korea (NRF) funded by the Ministry of Education [Grant No. 2021R1F1A105053912], and the Natural Science Foundation of Jilin Province [Grant No. 20240101295JC]. This research was supported by the Commercialization Promotion Agency for R&D Outcomes (COMPA), funded by the Ministry of Science and ICT (MSIT) (1711198544, Development of analytical instrumentation for electromagnetics/optics/thermal characteristics under extreme environments). This research was also supported by the National Research Foundation of Korea (NRF) (grant number RS-2023-00250178) the academic research program of Chungbuk National University in 2024. [Correction added on January 7, 2026, after first online publication: Funding information has been added in the acknowledgment section in this version.]

Conflict of Interest

The authors declare no conflict of interest.

Data Availability Statement

The data that support the findings of this study are available from the corresponding author upon reasonable request.

Keywords

exchange bias, magnetic heterostructures, spin dynamics, spintronics, terahertz emission

Received: October 4, 2025
Revised: December 14, 2025
Published online: December 31, 2025

---

[1] T. Kampfrath, M. Battiato, P. Maldonado, G. Eilers, J. Nötzold, S. Mährlein, V. Zbarsky, F. Freimuth, Y. Mokrousov, S. Blügel, M. Wolf, I. Radu, P. M. Oppeneer, M. Münzenberg, *Nat. Nanotechnol.* **2013**, *8*, 256.
[2] T. Seifert, S. Jaiswal, U. Martens, J. Hannegan, L. Braun, P. Maldonado, F. Freimuth, A. Kronenberg, J. Henrizi, I. Radu, E. Beaurepaire, Y. Mokrousov, P. M. Oppeneer, M. Jourdan, G. Jakob, D. Turchinovich, L. M. Hayden, M. Wolf, M. Münzenberg, M. Kläui, T. Kampfrath, *Nat. Photonics* **2016**, *10*, 483.
[3] D. M. Mittleman, *J. Appl. Phys.* **2017**, *122*, 230901.
[4] L. Cheng, Z. Li, D. Zhao, E. E. M. Chia, *APL Mater.* **2021**, *9*, 070902.
[5] I. Ilyakov, A. Brataas, T. V. A. G. de Oliveira, A. Ponomaryov, J. C. Deinert, O. Hellwig, J. Faßbender, J. Lindner, R. Salikhov, S. Kovalev, *Nat. Commun.* **2023**, *14*, 7010.
[6] J. Walowski, M. Münzenberg, *J. Appl. Phys.* **2016**, *120*, 140901.
[7] H. J. Song, T. Nagatsuma, *IEEE Trans. Terahertz Sci. Technol.* **2011**, *1*, 256.
[8] H. Elayan, O. Amin, R. M. Shubair, M. S. Alouini, *Terahertz Communication: The Opportunities of Wireless Technology Beyond 5G*, IEEE, New York City **2018**, pp. 1–5.
[9] D. D. Arnone, C. M. Ciesla, A. Corchia, S. Egusa, M. Pepper, J. M. Chamberlain, C. Bezant, E. H. Linfield, R. Clothier, N. Khammo, *Proc. SPIE* **1999**, *3828*, 209.
[10] Z. Yan, L. G. Zhu, K. Meng, W. Huang, Q. Shi, *Trends Biotechnol.* **2022**, *40*, 816.
[11] E. Beaurepaire, G. M. Turner, S. M. Harrel, M. C. Beard, J. Y. Bigot, C. A. Schmuttenmaer, *Appl. Phys. Lett.* **2004**, *84*, 3465.
[12] L. Huang, J. W. Kim, S. H. Lee, S. D. Kim, V. M. Tien, K. P. Shinde, J. H. Shim, Y. Shin, H. J. Shin, S. Kim, J. Park, S. Y. Park, Y. S. Choi, H. J. Kim, J. I. Hong, D. E. Kim, D. H. Kim, *Appl. Phys. Lett.* **2019**, *115*, 142404.
[13] L. Huang, S. H. Lee, S. D. Kim, J. H. Shim, H. J. Shin, S. Kim, J. Park, S. Y. Park, Y. S. Choi, H. J. Kim, J. I. Hong, D. E. Kim, D. H. Kim, *Sci. Rep.* **2020**, *10*, 15843.
[14] T. Seifert, U. Martens, S. Günther, M. A. W. Schoen, F. Radu, X. Z. Chen, I. Lucas, R. Ramos, M. H. Aguirre, P. A. Algarabel, A. Anadón, H. S. Körner, J. Walowski, C. Back, M. R. Ibarra, L. Morellón, E. Saitoh, M. Wolf, C. Song, K. Uchida, M. Münzenberg, I. Radu, T. Kampfrath, *SPIN* **2017**, *7*, 1740010.
[15] G. Torosyan, S. Keller, L. Scheuer, R. Beigang, E. Th Papaioannou, *Sci. Rep.* **2018**, *8*, 1311.
[16] X. Wu, H. Wang, H. Liu, Y. Wang, X. Chen, P. Chen, P. Li, X. Han, J. Miao, H. Yu, C. Wan, J. Zhao, S. Chen, *Adv. Mater.* **2022**, *34*, 2204373.
[17] Y. Zhao, A. Gayen, L. Huang, X. You, N. L. Thi, Q. Mustaghfiroh, F. Rahmani, P. V. Gaikwad, P. D. H. Yen, J. H. Shim, D. E. Kim, H. J. Shin, J. Park, C. Wan, O. Xiang, H. G. Piao, K. H. Kim, J. Bang, H. S. Lee, K. W. Kim, D. H. Kim, *Adv. Optical Mater.* **2024**, *12*, 2302571.
[18] C. Zhou, Y. P. Liu, Z. Wang, S. J. Ma, M. W. Jia, R. Q. Wu, L. Zhou, W. Zhang, M. K. Liu, Y. Z. Wu, J. Qi, *Phys. Rev. Lett.* **2018**, *121*, 086801.
[19] M. B. Jungfleisch, Q. Zhang, W. Zhang, J. E. Pearson, R. D. Schaller, H. Wen, A. Hoffmann, *Phys. Rev. Lett.* **2018**, *120*, 207207.
[20] X. Liu, A. Chanana, U. Huynh, F. Xue, P. Haney, S. Blair, X. Jiang, Z. V. Vardeny, *Nat. Commun.* **2020**, *11*, 323.
[21] N. Tesařová, P. Němec, E. Rozkotová, J. Zemen, T. Janda, D. Butkovičová, F. Trojánek, K. Olejník, V. Novák, P. Malý, T. Jungwirth, *Nat. Photonics* **2013**, *7*, 492.
[22] L. Huang, Y. Cao, H. Qiu, H. Bai, L. Liao, C. Chen, L. Han, F. Pan, B. Jin, C. Song, *Nat. Commun.* **2024**, *15*, 7227.
[23] Z. Chu, J. Yang, Y. Li, K. Hwangbo, J. Wen, A. R. Bielinski, Q. Zhang, A. B. F. Martinson, S. O. Hruszkewycz, D. D. Fong, X. Xu, M. R. Norman, A. Bhattacharya, H. Wen, *Sci. Adv.* **2024**, *10*, ads8601.
[24] A. L. Chekhov, Y. Behovits, J. J. F. Heitz, M. A. Syskaki, S. Jaiswal, O. Gueckstock, B. R. Serrano, A. Ruge, J. Kredl, M. Wolf, M. Münzenberg, G. Jakob, M. Kläui, T. S. Seifert, T. Kampfrath, *Sci. Adv.* **2025**, *11*, adq7741.
[25] Q. Zhang, Z. Luo, H. Li, Y. Yang, X. Zhang, Y. Wu, *Phys. Rev. Appl.* **2019**, *12*, 054027.
[26] T. S. Seifert, U. Martens, F. Radu, M. Ribow, M. Berritta, L. Nádvorník, R. Starke, T. Jungwirth, M. Wolf, I. Radu, M. Münzenberg, P. M. Oppeneer, G. Woltersdorf, T. Kampfrath, *Adv. Mater.* **2021**, *33*, 2007398.
[27] H. Cheng, Y. Wang, Z. Liu, X. Jia, Q. Huang, Y. Lu, *Nanophotonics* **2023**, *12*, 2145.
[28] R. Mandal, R. Momma, K. Ishibashi, S. Iihama, K. Suzuki, S. Mizukami, *NPG Asia Mater* **2024**, *16*, 30.
[29] J. Nogués, I. K. Schuller, *J. Magn. Magn. Mater.* **1999**, *192*, 203.
[30] R. L. Stamps, *J. Phys. D: Appl. Phys.* **2000**, *33*, R247.
[31] V. Skumryev, S. Stoyanov, Y. Zhang, G. Hadjipanayis, D. Givord, J. Nogués, *Nature* **2003**, *423*, 850.
[32] J. Nogués, J. Sort, V. Langlais, V. Skumryev, S. Surinach, J. S. Muñoz, M. D. Baró, *Phys. Rep.* **2005**, *422*, 65.
[33] B. Dieny, V. S. Speriosu, S. S. P. Parkin, B. A. Gurney, D. R. Wilhoit, D. Mauri, *Phys. Rev. B* **1991**, *43*, 1297.
[34] J. S. Moodera, L. R. Kinder, T. M. Wong, R. Meservey, *Phys. Rev. Lett.* **1995**, *74*, 3273.
[35] C. Binek, A. Hochstrat, X. Chen, P. Borisov, W. Kleemann, B. Doudin, *J. Appl. Phys.* **2005**, *97*, 10C514.

[36] H. F. Liu, S. S. Ali, X. F. Han, *Chin. Phys. B* **2014**, *23*, 077501.
[37] S. Peng, D. Zhu, W. Li, H. Wu, A. J. Grutter, D. A. Gilbert, J. Lu, D. Xiong, W. Cai, P. Shafer, K. L. Wang, W. Zhao, *Nat. Electron.* **2020**, *3*, 757.
[38] Y. Saito, F. N. Kholid, E. Karashtin, I. Pashenkin, R. V. Mikhaylovskiy, *Phys. Rev. Appl.* **2023**, *19*, 064040.
[39] X. Ma, F. Fang, Q. Li, J. Zhu, Y. Yang, Y. Z. Wu, H. B. Zhao, G. Lüpke, *Nat. Commun.* **2015**, *6*, 8800.
[40] R. V. Mikhaylovskiy, E. Hendry, A. Secchi, J. H. Mentink, M. Eckstein, A. Wu, R. V. Pisarev, V. V. Kruglyak, M. I. Katsnelson, T. Rasing, A. V. Kimel, *Nat. Commun.* **2015**, *6*, 8190.
[41] J. H. Shim, A. A. Syed, Y. Shin, J. W. Kim, H. G. Piao, S. H. Lee, K. M. Lee, J. R. Jeong, D. H. Kim, D. E. Kim, *Commun. Phys.* **2020**, *3*, 74.
[42] C. Li, B. Fang, L. Zhang, Q. Chen, X. Xie, N. Xu, Z. Zeng, Z. Wang, L. Fang, *Phys. Rev. Appl.* **2021**, *16*, 024058.
[43] W. Zhang, M. B. Jungfleisch, W. Jiang, J. E. Pearson, A. Hoffmann, F. Freimuth, Y. Mokrousov, *Phys. Rev. Lett.* **2014**, *113*, 196602.
[44] L. Frangou, S. Oyarzún, S. Auffret, L. Vila, S. Gambarelli, V. Baltz, *Phys. Rev. Lett.* **2016**, *116*, 077203.
[45] Z. Chen, J. W. Luo, L. W. Wang, *Sci. Adv.* **2023**, *9*, 1618.
[46] Y. Yang, Y. Xu, K. Yao, Y. Wu, *AIP Adv.* **2016**, *6*, 065203.
[47] X. Wang, C. Wan, Y. Liu, Q. Shao, H. Wu, C. Guo, C. Fang, Y. Guang, W. Yang, C. He, B. Tao, X. Zhang, T. Ma, J. Dong, Y. Zhang, J. Feng, J. Xiao, K. L. Wang, G. Yu, X. Han, *Phys. Rev. B* **2020**, *101*, 144412.
[48] J. Xu, M. Jia, C. Zhou, Q. Li, P. Shafer, G. Chen, M. Yang, A. T. N'Diaye, E. Arenholz, Z. Qiu, Y. Wu, *Phys. Rev. B* **2022**, *106*, 134425.
[49] D. V. Averyanov, I. S. Sokolov, A. N. Taldenkov, O. E. Parfenov, I. A. Karateev, O. A. Kondratev, A. M. Tokmachev, V. G. Storchak, *ACS Nano* **2022**, *16*, 19482.
[50] J. H. Shim, A. A. Syed, J. I. Kim, H. G. Piao, S. H. Lee, S. Y. Park, Y. S. Choi, K. M. Lee, H. J. Kim, J. R. Jeong, J. I. Hong, D. E. Kim, D. H. Kim, *Sci. Rep.* **2020**, *10*, 6355.